Electronic Supplementary Material (ESI) for Physical Chemistry Chemical Physics.
This journal is © the Owner Societies 2014

SUPPORTING INFORMATION (SI)

Hexagonal Ice Stability and Growth in the presence of Glyoxal and Secondary Organic Aerosols

Vangelis Daskalakis* and Marios Hadjicharalambous

Cyprus University of Technology, Department of Environmental Science and Technology, P.O. Box 50329, 3603 Limassol – Cyprus.

***Corresponding Author:** Vangelis Daskalakis

Tel: +357 25002458, Fax. +357 25002820. E-mail: evangelos.daskalakis@cut.ac.cy

Contents

1. **Force Field parameters for the organics (glyoxal, glyoxal hydrates and dimer, as well as the oxalic acid)**
2. **Evaluation of the adopted Force Fields**
3. **Superheating at the target temperature of 320K**
4. **Selection process for the supercooling initial conformations**
5. **Partial growth of ice crystals in the multi-compound systems in the presence of CO_2**

KEYWORDS: Ice 1_h, atmospheric physics, glyoxal, secondary organic aerosol, superheating, supercooling, total dipole moment.

1. Force Field parameters for the organics (glyoxal, glyoxal hydrates and dimer, as well as the oxalic acid).

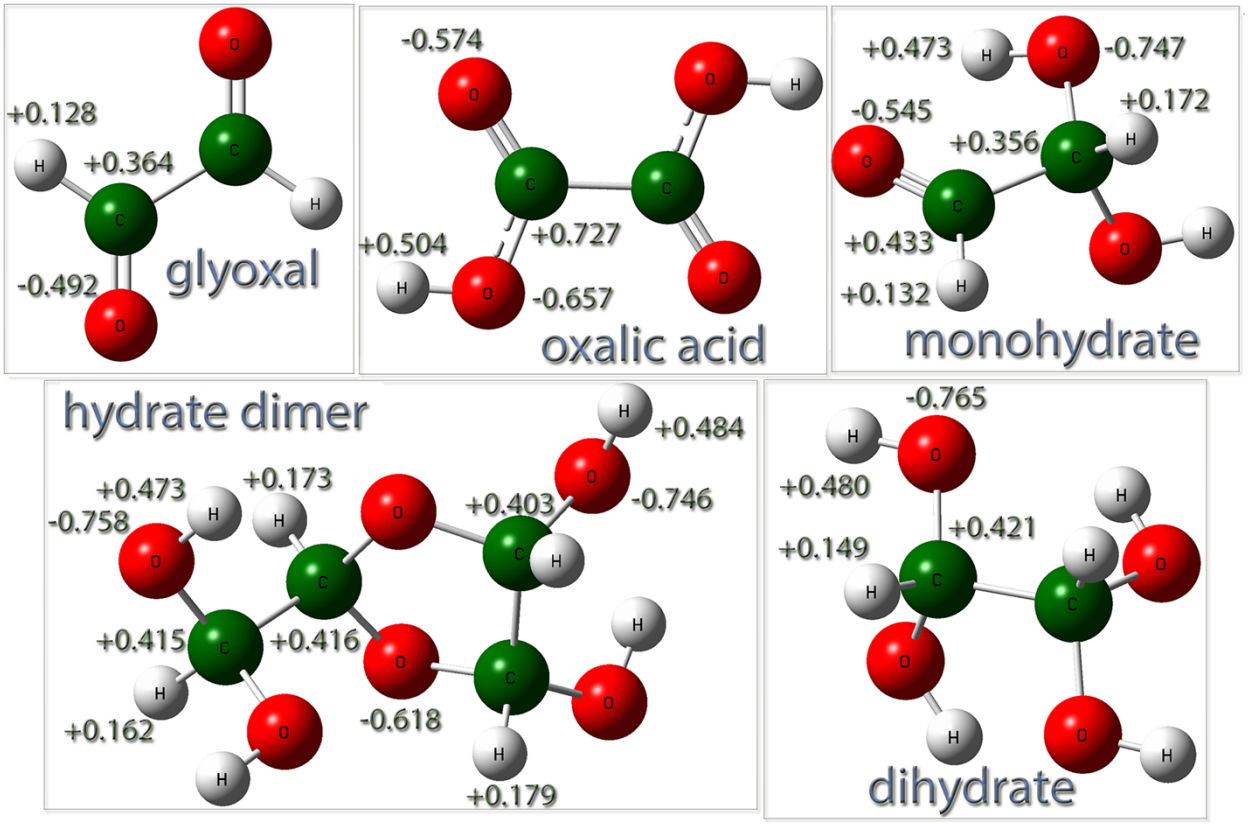

Figure S1. Geometry optimized glyoxal and Secondary Organic Aerosol at the b3lyp/6-311g(d,p) level of theory. Charges from NBO analysis on each atom are shown in green.

Glyoxal and secondary organic aerosol potential parameters, such as partial atomic charges from Natural Bond Orbital (NBO) analysis were obtained by a DFT b3lyp/6-311g(d,p) based geometry optimization of each organic molecule (**Figure S1**). Additional potential parameters for the organic molecules were derived from the OPLS-2005 force field [1]. These potential parameters were used throughout our simulations. Especially for alcohols we compared the partial charges and Lennard-Jones parameters on selected atoms to make sure for the correct hydrogen bonding strengths in the alcohol-water interface [2]. *Trans*-glyoxal is the lowest energy isomer of glyoxal [3], but both isomers were used for

our Molecular Dynamics (MD) models as initial input structures. During the MD simulations we have observed *trans* to *cis*-glyoxal and vice-versa transitions.

2. Evaluation of the adopted Force Fields.

The NE6 [4] potential for the water molecules was implemented. The six-site water potential NE6 succeeds in predicting the nucleation process at conditions close to experimental reality [5-6]. NE6 predicted melting point at 289K was calculated in a recent study using a combination of a Gibbs-Duhem integration and free energy calculations, and determined by a direct coexistence of ice and liquid [7].

Adsorbates	**FEP Free Energies of Solvation [this study]**	**DFT/ x3lyp [12]**
Glyoxal	-5.34±0.08	-4.14
Monohydrate	-11.56±0.17	-10.56
Dihydrate	-16.83±0.16	-15.34
Hydrate Dimer	-19.51±0.20	-18.63

Table S1. Free Energies of Solvatioon for glyoxal and secondary organic aerosol in kcal/mol.

Methods for calculating relative free energies (ΔF) or energies of solvation using free energy perturbation (FEP) [8] involve "annihilation", in which a selected molecule is removed from the system [9]. FEP calculations were performed using Desmond 2013.1 software. For the free energies of solvation of the organics in water, the protocol included solvation in a box of SPC [10] water molecules with a buffer distance of at least 12Å. The system went through a relaxation process that included two minimizations followed by 4 short NVT/ NpT molecular dynamics simulations. The production simulation (NpT, T=298K, P=1 atm) was run for 2 ns for each lambda window, and 12 windows were used for each perturbation,

involving “annihilation” of the organic molecule. Results were collected and analyzed based on the Bennett acceptance ratio method [11]. The absolute solvation energy per molecule is derived for the different organics at 298K. The results are shown on **Table S1**. Custom NBO charges from the DFT geometry optimization results were used for the organics. The free energies of solvation are consistent with the DFT derived energies at the x3lyp level of theory, as well as experimental observations [12] even with the SPC potential for water. For the oxalic acid, in MD simulations we do not consider the dissociation of the acid, hence the absolute free energy of solvation from FEP calculations cannot be directly associated with the x3lyp or experimental values in the literature [12].

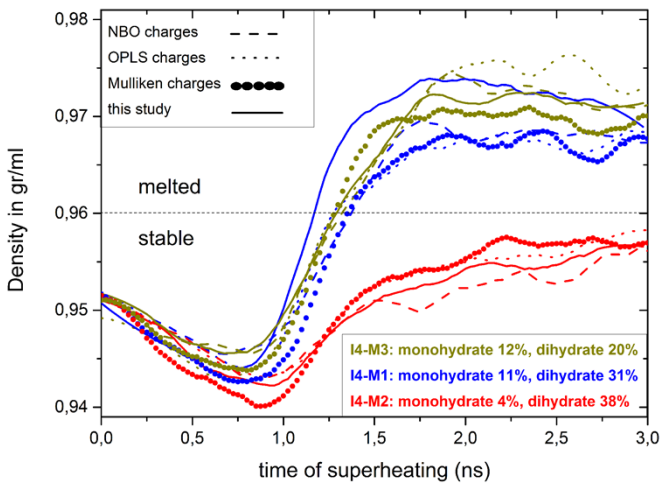

Figure S2. Superheating at 296K for the I4-M1, I4-M2 and I4-M3 multi-compound aerosols. Diverse charges have been used for the organics (NBO, Mulliken and native OPLS-2005). A cut-off distance at 1.1 nm is used for all except the solid lines for which the cut-off distance is set to 0.65nm.

Additional superheating dynamics were performed for the I4-47.0 nm^3 ice 1_h crystal in contact with OM phases of organic mixtures (glyoxal, monohydrate, hydrate dimer, dihydrate and oxalic acid) in the different -M1 (2.3%), -M2 (3.0%) and -M3 (3.2%) enrichments. Organic charges were customized according to Mulliken and NBO based values at the b3lyp/6-311g(d,p) level (this study), NBO charges at the same level of theory with the Polarizable Continuum Model (PCM) implicit solvation, as well as the native OPLS-2005 charges. The cut-off distance for the non-bonded interactions was set at 1.1 nm. The results for the superheating dynamics at the target temperature of 296K converge (**Figure S2**), as all these sets of charges, even with different absolute values, reflect qualitatively the correct polarization of

each organic molecule (total dipole moment of the OM respective phase), as well as the hydrogen bonding interactions, both being important for solvent-solute interactions.

3. Superheating at the target temperature of 320K

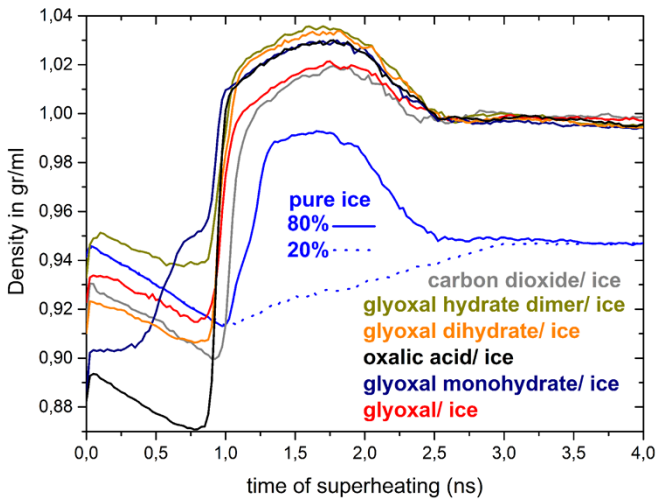

Figure S3. Density change profiles of the I1-41.0, I2-51.2 nm^3 and I3-61.6 nm^3 ice 1_h crystals at 7.6-10.8% w/w average enrichments in glyoxal and its secondary organic aerosol (SOA). The density profiles are averaged over all enrichments for each binary sample.

On **Figure S3** we depict the superheating dynamics of all the binary systems treated at this study, at the target temperature of 320K, in terms of density changes. These density time series evidence the collapse (melting) of the ice 1_h crystals for every binary system. We can observe that all the trajectories of the enriched crystals led to melting, exerting a density increase trend. For each binary mixture or pure ice 1_h crystals we have averaged 60 trajectories of the different ice 1h crystal volumes (I1-41.0, I2-51.2 and I3-61.6 nm^3) and subsequently smoothed the curves. This is done as the density versus time plots for these 60 trajectories per binary system do not differ much, exhibiting almost the same profile. The glyoxal monohydrate enrichments start melting earlier than any other probed at the target temperature of 320K, as it is the case also for 296K (see main manuscript for discussion). Both pure ice 1_h density change profiles (solid and dashed blue lines) converge to a final density of 0.95 gr/ml, even if the solid line is associated with the 80% of the trajectories leading to crystal collapse. Although the same final

density, visual observation of the phase transition trajectories, showed many ice nuclei still present in these trajectories, while their spatial distribution evidences a highly amorphous instead of crystalline ice phase. It is due to this behavior that a less pronounced density change profile is observed for the latter pure ice melting trajectories. We have to note that this is a unique behavior only for the pure ice samples and it is not observed for the OM enriched samples at this extend, where the density transition from solid to liquid is more pronounced, as it was also found by visual probing.

4. Selection process for the supercooling initial conformations

Several snapshots from a superheating run of the ice-glyoxal binary sample are shown on **Figure S4**. We should note though, that this figure is rather a rough illustration of the dynamics of one trajectory and no important conclusions should be drawn. We select two conformations around the temperature where the phase transition fully occurs in each superheating trajectory (320K). This yields 2x20=40 input conformations for the supercooling simulations per each system, similar to those of **Figure S4** at 1.1 and 2.0 ns. There is evidence that certain organic species (glyoxal monohydrate and oxalic acid) disturb the electrostatic potential of the ice 1_h even in regions further away from their organic phase (see results on the main manuscript based on electrostatic potential maps [13] averaged over time for each ice-OM sample). The ice 1_h structure in these regions, even further away from the organic phase, would become vulnerable to the temperature increase and start collapsing in addition to the OM/ ice contact region. This is visible in several trajectories of the monohydrate and the oxalic acid adsorbate phases in contact with ice crystals under the superheating dynamics (296K, 320K). It is unlikely for those regions to contain any nucleation seeds upon superheating. On the other hand, such a behavior is not observed for the rest of the organic species. Thus, nucleation seeds present in the initial

structures for the ice growth dynamics (supercooling at 250K), are likely to be present in regions where ice 1_h lattice is not disturbed by the effects of the organic phase.

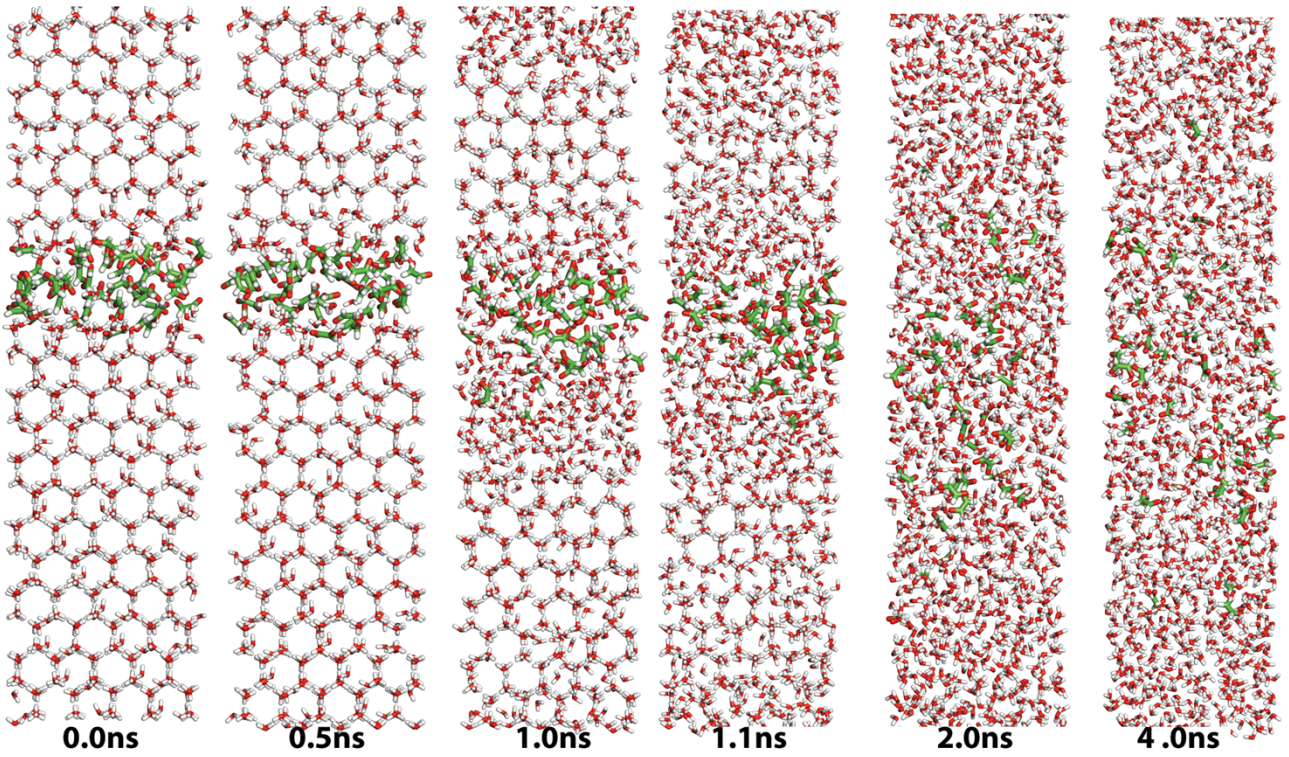

Figure S4. Time evolution of part of an ice 1_h – glyoxal conformation throughout the superheating dynamics. Organic molecules are centered in these snapshots for visualization purposes only, without any effects on the superheating dynamics. Molecules are depicted with green carbon atoms, red oxygens and white hydrogens.

5. Partial growth of ice crystals in the multi-compound systems in the presence of CO_2

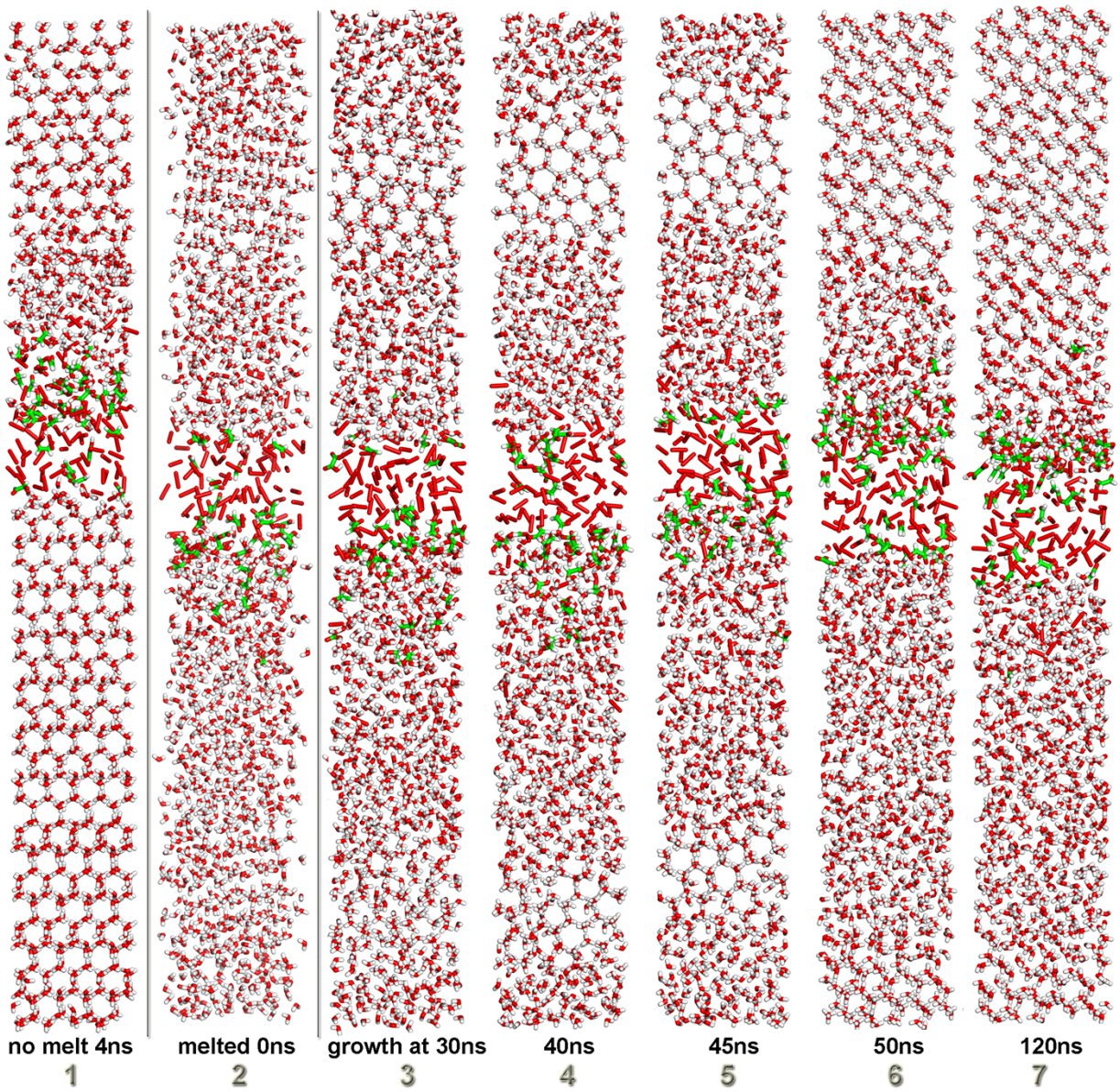

Figure S5. (1) Equilibrated Ice crystal in the presence of CO_2 under superheating dynamics, (2-7) Time evolution of the multi-compound samples throughout the supercooling dynamics at 250K from a seeded aerosol (frame 2) to 120ns (frame 7). CO_2 is depicted in red, organic molecules are depicted with green carbon atoms, red oxygens and white hydrogens, water with red oxygens and white hydrogens as well.

Figure S5 shows snapshots – configuration structures from the superheating (frame 1) and supercooling (frames 2-7) dynamics for a multi-compound system in the presence of CO_2. In the first snapshot the structure is typical of the orientation of both OM and CO_2 phases in multi-compound systems throughout equilibration/ relaxation and the superheating dynamics; an orientation that leads to decreased interactions between OM and water by mixing with CO_2. The ice 1_h structure in the upper part of frame 1 is less ordered with the ice phase to start mixing with the OM, while on the lower part a CO_2 layer prohibits such a mixing. A CO_2 nucleation (bubble) is more evident for the rest of the frames, while the organic species are concentrated in the interface between water (ice/ liquid) and the bubble (gas). Although this figure is rather a rough illustration of the dynamics of one trajectory and no important conclusions should be drawn, we have to note that we clearly identify the occurrence of a CO_2 gas phase in red coloring.

Bibliographic References

1. W.L. Jorgensen, D.S. Maxwell and J. Tirado-Rives. *J. Am. Chem. Soc.* 1996, **118**, 11225-11236.
2. R.D. Nutt and J.A. Stone. *J. Chem. Phys*., 2003, **119**, 5670-5679.
3. F. Bulat and A. Toro-Labbé. *Chem. Phys. Lett.,* 2002, **354**, 508-517.
4. H. Nada, P.J.M. van der Eerden, Jan. *J. Chem. Phys*. 2003, **118**, 7401-7413.
5. H. Nada and Y. Furukawa. *J. Cryst. Growth,* 2005, **283**, 242-256.
6. I. Gladich, W. Pfalzgraff, O. Maršálek, P. Jungwirth, M. Roeselová and S. Neshyba. *Phys. Chem. Chem. Phys.* 2011, **13**, 19960-19969.
7. J.L.F. Abascal, R.G. Fernández, C. Vega and M.A. Carignano. *J. Chem. Phys.* 2006, **125**, 166101.
8. R.W. Zwanzig. *J. Chem. Phys.,* 1954, **22**, 1420-1426.
9. D. Shivakumar, J. Williams, Y. Wu, W. Damm, J. Shelley and W.J. Sherman. *Chem. Theory Comput.,* 2010, **6 (5)**, 1509–1519.
10. C.D. Berweger, W.F. van Gunsteren and F. Müller-Plathe. *Chem. Phys. Lett.,* 1995, **232**, 429-436.
11. C.H. Bennett. *J. Comp. Phys.* 1976, **22**, 245–268.
12. C. Tong, M. Blanco, W.A. Goddard III and J.H. Seinfeld. *Environ. Sci. Technol*., 2006, **40 (7)**, 2333–2338.
13. A. Aksimentiev and K. Schulten. *Biophys. J.,* 2005, ***88***, 3745-3761.